BAR-ILAN UNIVERSITY

High-resolution single-pixel Computational Tomography with X-ray scattering radiation

Adi Ben Yehuda

Submitted in partial fulfillment of the requirements for the Master's Degree

in the Department of Physics, Bar-Ilan University

Ramat-Gan, Israel 2023

This work was carried out under the supervision of

Prof. Sharon Shwartz

Department of Physics, Bar-Ilan University

Table of Contents

Abstract

Commercial x-ray imaging modalities measure the x-rays that pass through the body, which are used to create a detailed image of the patient's body or organs. When the x-ray radiation interacts with the atoms in the patient's body it scatters and degrades the image's quality by reducing its contrast and sharpness. For this reason, scattered x-ray radiation is generally considered as a source of noise thus modern x-ray scanners endeavor to minimize its impact by placing grids and collimators between the patient's body and the camera. This allows the images to be in higher contrast but at the price of more harmful radiation exposure as the patient, which needs to be exposed to more radiation when a major part of it is blocked before reaching the camera. The impact of such effects is even more dominant in medical computed tomography (CT) scans, as multiple x-ray images are required to be taken in order to reconstruct a 3D image.

Multiple attempts to use the scattered radiation for imaging were developed in the past but none of them are suited for medical imaging as the resolution achieved by such devices is too low in order to be used for biology purposes [1,2].

My research shows that it is possible to utilize the scattered radiation for high resolution imaging instead of blocking it in the imaging process. I employ the computational ghost imaging (CGI) method, which is from of single-pixel imaging method that had been shown to be more robust to scattering than standard imaging methods [3,4], as the spatial information is derived from the spatially modulated beam, which interacts with the object, rather than from the detector pixels.

I utilized an 80kVp x-ray source because it can be used for medicinal and biological imaging. In addition, I used a known mask created by Nano-Dimension [7] as I was able to use their 3D printer technology, typically used for printing electrical circuits with silver, to fabricate a mask from an image I generated in my computer. Developing a mask suitable for utilization with high-energy x-rays presents a significant challenge due to the increased penetration depth of radiation at these photon energy levels. To address this challenge, I employed silver as the mask material, leveraging its exceptional blocking properties to effectively attenuate the x-ray radiation. By strategically selecting silver as the mask material, I ensured the successful containment of a substantial amount of radiation, enabling precise control and manipulation during imaging processes.

With CGI I managed to reconstruct 20mm x 20mm, sub 200µm scatter image of a cow bone. Because the image had too many pixels in comparison to the number of measurements, I was able to take in a reasonable time, the final picture was low in quality and in contrast. To solve this, I was able to adopt a deep neural network (DNN) based algorithm (GIDC) [8] to my use. To get more information about the object I reconstructed a CT 3D image that can be used to diagnose complicated medical conditions in patients. I rotated the object with a rotation stage and reconstructed 28 different scatter images. Then I used an iterative algorithm SART-TV [9] to reconstruct the 3D CT image.

Ultimately, I reconstructed with high energy x-ray scattered radiation a 3D CT image of large mammal bone with sub 200µm resolution, which is better than most x-ray imaging modalities. My research reveals a promising technique to incorporate scattered radiation data in CT scans, resulting in improved image resolution and reduced radiation dosage for patients. In my research I prove that scattered x-ray radiation can be used to reconstruct high-resolution computed tomography images with biological samples.

1. Motivation

Commercial x-ray scanners operate on the same physical principle that Wilhelm Roentgen demonstrated in 1895 when he used x-rays to image his hand of his wife [10]. The x-rays pass through the object and are absorbed to varying degrees by the different structures, creating an image that shows the internal composition of the object. For example, in medical imaging, denser structures such as bones absorb more x-rays and appear white on the image, while softer tissues like muscles and organs absorb fewer x-rays and appear darker. This very simple concept has proven useful and robust, making x-rays one of the most valuable medical and industrial imaging modalities. However, it became apparent soon after x-rays were first used for imaging that the image quality was significantly degraded in many practical scenarios where the density variations of the organs were small or when the volume of the object is significant [11–14]. When x-rays interact with the electrons in the object, they are not only absorbed but are also scattered introducing significant blurring and distortions of the images. To mitigate the impact of scattered radiation on the image quality grids or collimators are used, but these tools also increase the radiation dose leading to a significant increase in the risk of radiation damage [15–20]. Despite the successful application of those devices their ability to reduce scattering is limited and might be insufficient for scenarios where the contrast of the image is low or when a detailed picture of the object is required. Moreover, strong scattering can result in a significant portion of x-ray radiation not reaching the detector, leading to an increase in radiation damage that must be compensated for by higher radiation doses on the object leading to even higher radiation damage risks.

Despite numerous attempts to improve image quality and reduce radiation dose, scattering remains a major challenge [21–31], especially in CT scans since they target large volumes and low contrasts. Compton scattering in human tissues is stronger than the absorption for the photon energy range typically used for CT scans (80-150 keV), as illustrated in Fig.1 [32], which shows the absorption (the photoelectric effect) and the Compton scattering (the incoherent scattering) in cortical bones as a function of the photon energy of the x-ray beam. This plot clearly shows that current x-ray imaging techniques leave substantial amount of energy unused, necessitating higher doses to achieve adequate image quality [33,34].

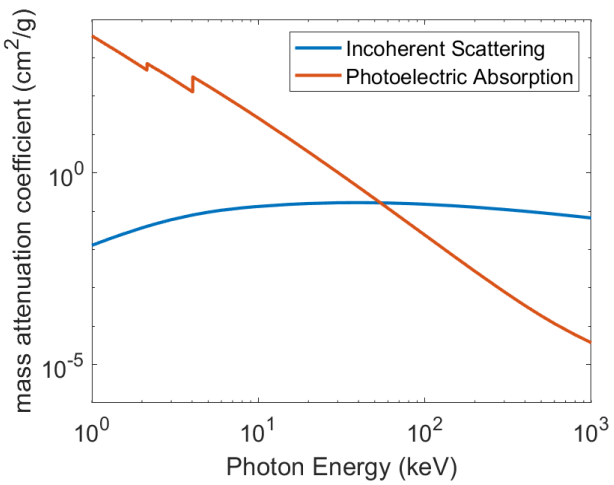

Fig. 1. Photon energy dependence of the cross-sections of photo absorption (orange) and Compton scattering (blue) in cortical bones. The incoherent scattering is stronger than the photoelectric absorption for photon energy range of 80-150 keV.

2. Background

2.1. Scattering x-ray radiation and Compton effect

In my experiment I utilized scattered radiation to reconstruct CT 3D images of a biological object. The major amount of radiation which scatters from the imaged object is due to the Compton effect. Compton scattering occurs when the incident x-ray photon is deflected from its original path by an interaction with an electron. The electron is ejected from its orbital position and the x-ray photon loses energy because of the interaction but continues to travel through the material along an altered path. Energy and momentum are conserved in this process. The energy shift depends on the angle of scattering and not on the nature of the scattering medium. Since the scattered x-ray photon has less energy, it has a longer wavelength and less penetrating than the incident photon.

The Compton effect was first observed by Arthur Compton in 1923 and this discovery led to his award of the 1927 Nobel Prize in Physics. The discovery is important because it demonstrates that light cannot be explained purely as a wave phenomenon. Compton's work convinced the scientific community that light can behave as a stream of particles (photons) whose energy is proportional to the frequency. Thus, the energy of the scattered photon decreases with increasing scattered photon angle. The change in wavelength of the scattered photon is given by:

$$\boldsymbol{\lambda' - \lambda = \frac{h}{m_e c}(1 - \cos(\theta))} \qquad \textbf{(1),}$$

And the differential cross section of the scattered radiation is given by the Klein-Nishina formula [35] :

$$\boldsymbol{\frac{d\sigma}{d\Omega} = \frac{1}{2} r_e^2 \left(\frac{\lambda}{\lambda'}\right)^2 \left[\frac{\lambda}{\lambda'} + \frac{\lambda'}{\lambda} - \sin^2(\theta)\right]} \qquad \textbf{(2),}$$

which provides an accurate prediction of the angular distribution of x-rays and gamma-rays that are incident upon a single electron.

$\boldsymbol{\frac{d\sigma}{d\Omega}}$ is the differential cross section, λ is the wavelength of incident x-ray photon, λ' is the wavelength of scattered x-ray photon, h is Planck's Constant, m_e is the mass of an electron at rest, c is the speed of light, θ is the scattering angle of the scattered photon and $\boldsymbol{r_e^2}$ is the classical electron radius.

2.2. Computational Ghost imaging

In my work I use the computational ghost imaging (CGI) method, since it has been shown to be more robust to scattering than standard imaging methods [3,4]. The ghost imaging (GI) approach has been investigated extensively in a broad range of wavelengths [6,36–41].The computational version of GI was proposed by Shapiro [42] and demonstrated first by Chan et al. with THz radiation [43], and with x-rays [6,37–41] later. While it has been demonstrated with transmitted [44–47], fluorescent [6], and reflected radiation, I apply it to incoherent scattered radiation for the first time.

The computational version of GI is performed as follows: a beam irradiates a known mask that induces intensity fluctuations in it. With the mask it is possible to get information on the object by measuring the amount of radiation detected after passing through it, fluorescent, or scattered from it. The photon count in the detector is dependent on the patten of the mask. The mask is changed for each of the realizations, thus in every realization the object is irradiated by a different pattern of x-rays. In my experiment, measurements are taken with a single-pixel detector, which is located 90 degrees the of object (Fig. 5). After completing the measurements for the entire set of realizations, sets of data that contain the photon counts are obtained by the single-pixel detector. Because the mask is known, the reconstruction of the image is possible after calculating the propagation of the beam at the object plain for each of the realizations.

2.3. Computational tomography

Computed tomography (CT) is a powerful medical imaging technique that has revolutionized the diagnosis and treatment of a wide range of diseases and injuries. The development of CT imaging was a significant milestone in the history of medical science and has had a profound impact on the field of radiology. The concept of tomography, or the imaging of a single plane through a three-dimensional object, was first introduced in 1917 by the Austrian mathematician Johann Radon. However, it was not until the development of computer technology in the 1960s that the first true CT scanner was created.

In 1972, British engineer Godfrey Hounsfield and his team at EMI Central Research Laboratories in England developed the first CT scanner, which used a series of rotating X-ray beams and sophisticated computer algorithms to generate detailed images of the body. The first

CT scanner took several hours to produce a single image, but it was still a significant breakthrough in medical imaging technology.

Over the next few decades, CT scanners became faster, more powerful, and more widely used in medical practice. The introduction of spiral or helical CT in the 1980s allowed for even faster imaging and higher resolution, and the development of multi-detector row CT scanners in the 1990s enabled even greater speed and accuracy. Today, CT imaging is an essential tool in diagnosing and monitoring a wide range of medical conditions, from cancer and heart disease to injuries and infections.

CT scans are often used in conjunction with other diagnostic tests to provide a more complete picture of a patient's health status, and to guide treatment decisions. CT imaging can detect changes in tissue density, identify the location and extent of tumors, and diagnose fractures or other bone injuries. In some cases, CT-guided biopsies or other minimally invasive procedures can be performed using CT imaging to guide the placement of needles or other instruments.

While CT imaging has revolutionized the field of medical imaging, it is not without risks. CT scans expose patients to ionizing radiation, which can increase the risk of cancer and other health problems over time. To minimize these risks, doctors must carefully weigh the potential benefits of CT imaging against the risks and use the lowest possible dose of radiation that is still effective. Despite these risks, CT imaging remains an essential tool in modern medicine.

In my work I present a new method of CT reconstruction. Which has the potential to reduce dose while also improving resolution by utilizing the advantage of CGI and an advanced DNN to reconstruct a CT image from x-ray scattered radiation.

3. Experimental and computational procedures

3.1. Mask production and calibration

The mask was created using a unique process by Nano-dimension, which utilizes a multi-material multi-layer 3D printer that the company typically uses for fabricating electrical circuits with silver and polymer. I designed the mask to have 1480x1480 pixels with transmission-absorption ratio of 1:1, and dimensions of 160mm x 160mm x 1.5mm with a feature size of 108μm.

To circumvent the potential inhomogeneity in the absorption of the mask, I measured its transmission using a low-resolution flat panel detector. I summed over all pixels in each measurement to normalize the data. To ensure accurate alignment with the manufacturing files on the computer, I used the same low-resolution flat panel detector to capture an image of the mask. I later established a correlation between this image and a low-resolution version of the manufacturing file, which enabled us to accurately locate the mask during the experiment.

3.2. Reconstruction procedure

The image is reconstructed by solving an inverse problem defined by the equation:

$$\boldsymbol{Ax = S} \qquad \textbf{(3),}$$

where the mask patterns are represented by the matrix A, for which every row is a single realization, the vector x is the response function of the object (either the transmission, the reflection, or scattering), and S is the detected signal. The reconstruction of the scatter image is done by solving the equation for the vector x.

Due to the absence of training data of x-ray scattering for high resolution images, I utilized a self-supervised deep neural network algorithm for reconstruction of the GI images. To accomplish this, I utilized the used a deep neural network constraint (GIDC) algorithm [8], which provides high performance reconstruction but is only able to reconstruct images with a number of pixels, that is a power of two in each axis. To meet this requirement, I resized my original image of the mask from 184 x 163 pixels to 128 x 128 pixels, resulting in a slight reduction in resolution. To find the vector x with a minimal number of realizations, and consequently to reduce the measurement time I had to optimize the GIDC far-field super-resolution reconstruction algorithm which was originally developed to improve resolution beyond the diffraction limit in visible light. I adopted it to my data by experimenting with it,

changing the loss rate and total variation (TV) [48] values which were calibrated to do a totally different task. Only then I was able to utilize its untrained, self-supervised deep neural network (DNN) advantages and generate high-resolution and high contrast results. The basic concept of the protocol is that a DNN with randomly initialized weights can recover an image more accurately by adding a conventional regularization term such as the TV. The minimization process of the loss function of GIDC is crucial in order to recover a good image. The weights are adjusted in every iteration with the constraint of the pre-determined TV value. The loss function is reformulated as follows:

$$\boldsymbol{T_{\varphi*} = argmin_{\varphi}\left|AT_{\varphi}(x_{DGI}) - S\right|^2 + \tau\mu\left[T_{\varphi}(x_{DGI})\right]}, \qquad \textbf{(4)}$$

where $T_{\varphi*}$ is the DNN, defined by a set of weights and biases parameters φ. The objective of GIDC is to find an optimal configuration φ^* for the neural network, which effectively constrains the network output to produce a 1D sequence $\tilde{S} = T_{\varphi}(x_{DGI})$, in accordance with the GI image formation physics as described by Eq.4. This reconstructed sequence should closely resemble the experimentally acquired bucket signal *S*, where x_{DGI} represents the *x* with normalized illumination patterns. μ represents TV coefficient and τ denotes the regularization parameter. This procedure allowed me to reconstruct a two-dimensional image that contains 16384 pixels constructed using 3468 mask iterations.

3.3. Experiment at lower photon energy

In the first experiment I modified the Rigaku SmatLab 9kW Type-F In-plane (x-ray diffraction) XRD machine in our lab for imaging. The x-ray source is 20keV while most of the spectrum is around 8keV which is emitted from the x-ray tubes copper anode. Since I used sandpaper for the mask, I measured it without the object and registered the profiles of the intensity at the object plane by acquiring the images at the various positions of the mask. The experimental setup of this step is described in Fig. 2(a), In the second step, which is depicted in Fig. 2(b), I inserted the object, the figure 7, made from a polylactic acid (PLA) as shown in Fig. 2(c). I measured the x-ray scattering with two energy resolving silicon drift detectors (SDDs) located at two different positions as is shown in Fig. 2(b). I then raster scanned the sandpaper and recorded the radiation, which was scattered from the object.

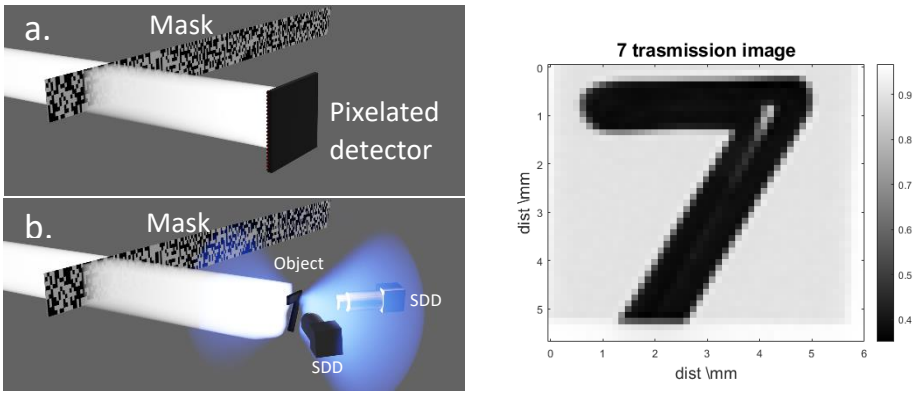

Fig. 2- Schematic of the experimentl setup and the sample. In step 1 (a), I measure the intensity patterns induced by the mask in the absence of the objects. In step 2 (b) I measure the radiation scattered off the object from both its sides. (c) The image obtained by direct imaging of the object.

Because the number of pixels in this experiment was only 31 by 40, I used the TVAL3 algorithm [5] for the image reconstruction to avoid the reduction in the resolution that is the results of the pixel resize required by the constraints of the GIDC code.

The image of the object reconstructed using the scattered radiation that was collected by the detectors for 3000 realizations is shown in Fig. 3. The number of pixels in the image is 1240 and at each realization I measured about 2×10^6 scattered photons from the object. Based on edge blurring, I estimate that the spatial resolution of my proof-of-principle experiment was about 150μm. This agrees with the width of the measured autocorrelation function Fig. 4 and indicates that further improvement of the spatial resolution is feasible by a simple reduction of the speckle size [6]. As shown in Fig. 3 each detector produced a slightly different image reconstruction, with areas containing more absorbing material appearing darker. For example, in Fig. 3(b) the detector is on the right side of the object resulted in a darker upper section of the image, as more material was present in that area. However, the bottom of the image was

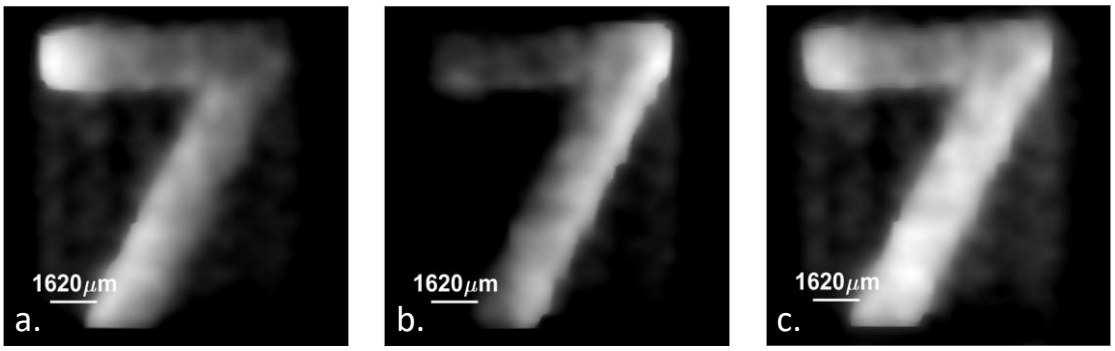

Fig. 3- Reconstruction images of the object with 3000 ralizations. Image (a) is the reconstraction of the left detector, image (b) is the recontraction of the right detector and image (c) is the combination of both images. This comparison show that different detector position resoult in different image reconstraction due to self absorption and scatter.

less affected by this effect due to the smaller size of the material, which blocked less radiation. By combining the images produced by each detector, I was able to produce a better, more homogeneous image, as I show in Fig. 3(c). The findings of the study highlight the critical role played by the position of the detector in relation to the object. This positioning can yield additional insights and should be considered when reconstructing images.

The spatial resolution of my method is determined by the width of the autocorrelation function of the mask that modulates the input x-ray beam [49]. The autocorrelation function of the mask is presented in Fig. 4(b), while the 1D horizontal and vertical projections are presented in Figs. 4(c) and 4(d), respectively. The autocorrelation function is nearly isotropic and the FWHM of the curve are 175 μm and 127 μm for the horizontal and vertical axes, respectively.

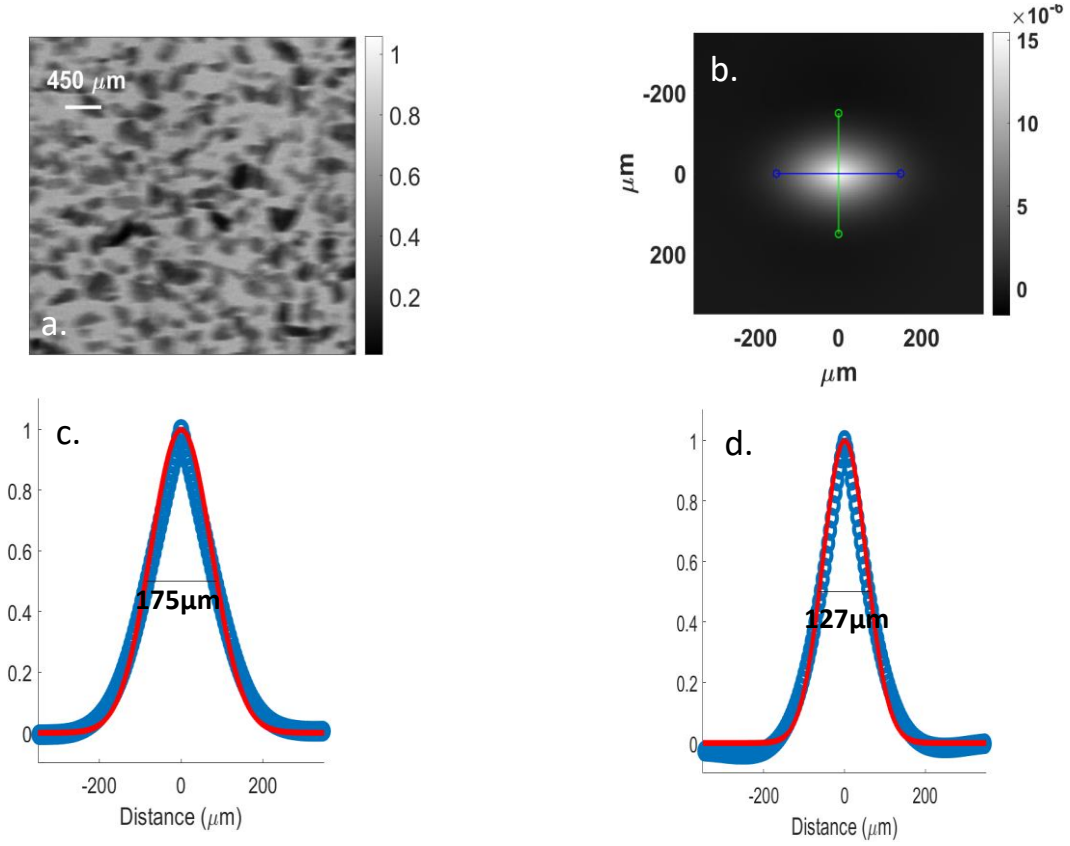

Fig. 4- Spatial resolution determanation. (a) Example of the reference data (the intensity fluctuations induced by the mask). (b) Autocorrelation function of the intensity pattern induced by the mask. The blue and green lines indicate the horizontal and vertical cross sections shown in (c) and (d). The blue dots are the measured data for the horizontal and vertical cross sections and the red curves are interpolation functions.

4. Experimental setup and CT acquisition at high photon energy

4.1. Experimental setup at high photon energy

I implemented the GI with scattered radiation scheme with the experimental setup illustrated in Fig. 5. It includes a 80kVp cone beam x-ray source, a 500 mm collimator (not shown) that is

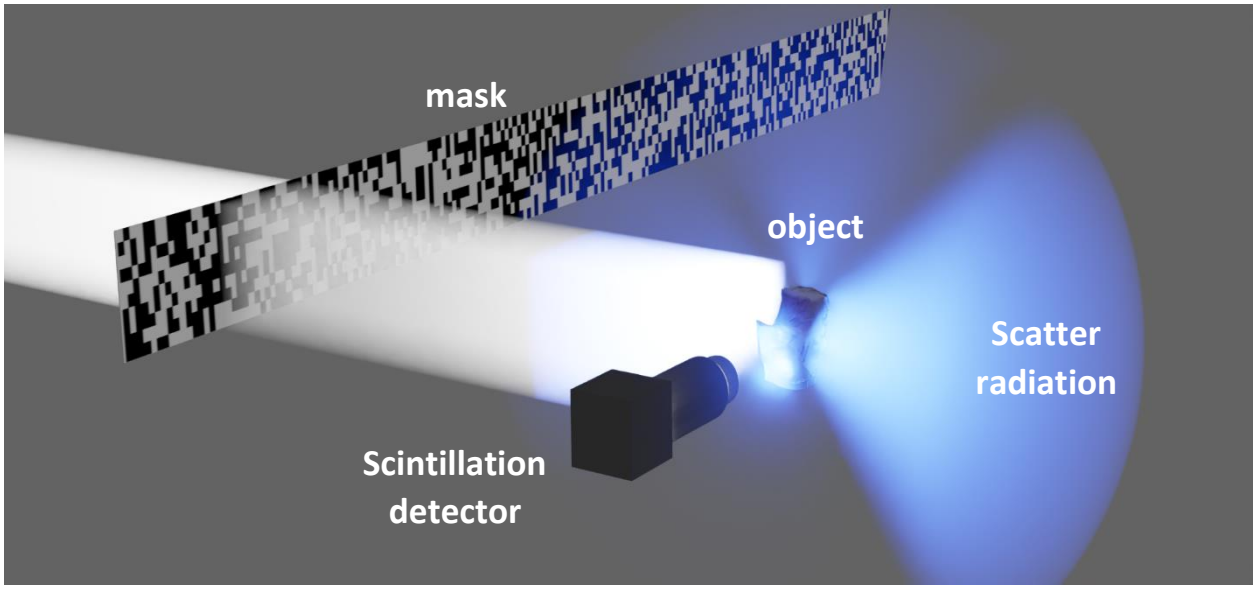

Fig. 5. Schematic of experimental setup. The silver mask irradiates the object (bone) with known random binary speckle patterns. The scattered x-ray radiation is then collected by a single pixel scintillation detector and the resulting signals are used to reconstruct a computational image from different angles as the object is rotated using a rotation stage (not shown).

mounted between the source and the object to minimize scattering from the surrounding environment, a silver mask that modulates the beam to create structured illumination on the object, a single-pixel scintillation detector for measuring the radiation scattered from the object, and a 360° rotation stage (not shown) for rotating the object during the measurements. The distance between the source and the mask is 1300 mm and the object is located 50 mm downstream of the mask. The spot size of the beam at the mask is about 17 x 19.5 mm^2.

The mask patterns are randomly distributed binary patterns with transmission-absorption ratio of 1:1, that are irradiated onto the object. High resolution x-ray SI techniques require the changing incident beam to have high contrast and small feature size which can be challenging at high photon energies, as photon penetration depth increases. To overcome this challenge, I adopted a technology made for electrical circuits 3D printing as it can provide 100µm printing resolution with silver as discussed in 3.1.

The scintillation detector is located 50 mm from the object. To demonstrate the ability of imaging from any angle, the detector was mounted at approximately 90° relative to the input beam since the differential cross section given by the Klein-Nishina formula (Eq.2) at this angle is small [35]

4.2. CT acquisition

To reconstruct a 3D image using tomographic reconstruction I used TIGRE, a tomographic iterative GPU (Graphics Processing Unit) based reconstruction toolbox [50]. To reconstruct a CT, projections of the object from different angles are essential. To achieve this, I rotated the object with a rotation stage and reconstructed 28 different scatter images. Then with TIGRE I used an iterative algorithm SART-TV [9] to reconstruct the 3D CT image.

I also took transmission x-ray pictures of the object and reconstructed a CT for reference.

5. Results

To validate my method and to benchmark its efficiency, resolution, and sensitivity against the transmission-based CT reconstruction, I reconstructed 3D images of a cortical bone using signals obtained from transmission, scattering, and their combination. The results of these reconstructions are presented in Figs. 6-8.

5.1. Isosurface images reconstruction

In Fig. 6 I present the isosurface (3-D surface representation of points with equal values in a 3-D data distribution) of the bone from the reconstructed images using all three methods. It is evident that the scatter reconstruction reveals finer features on the surface of the object

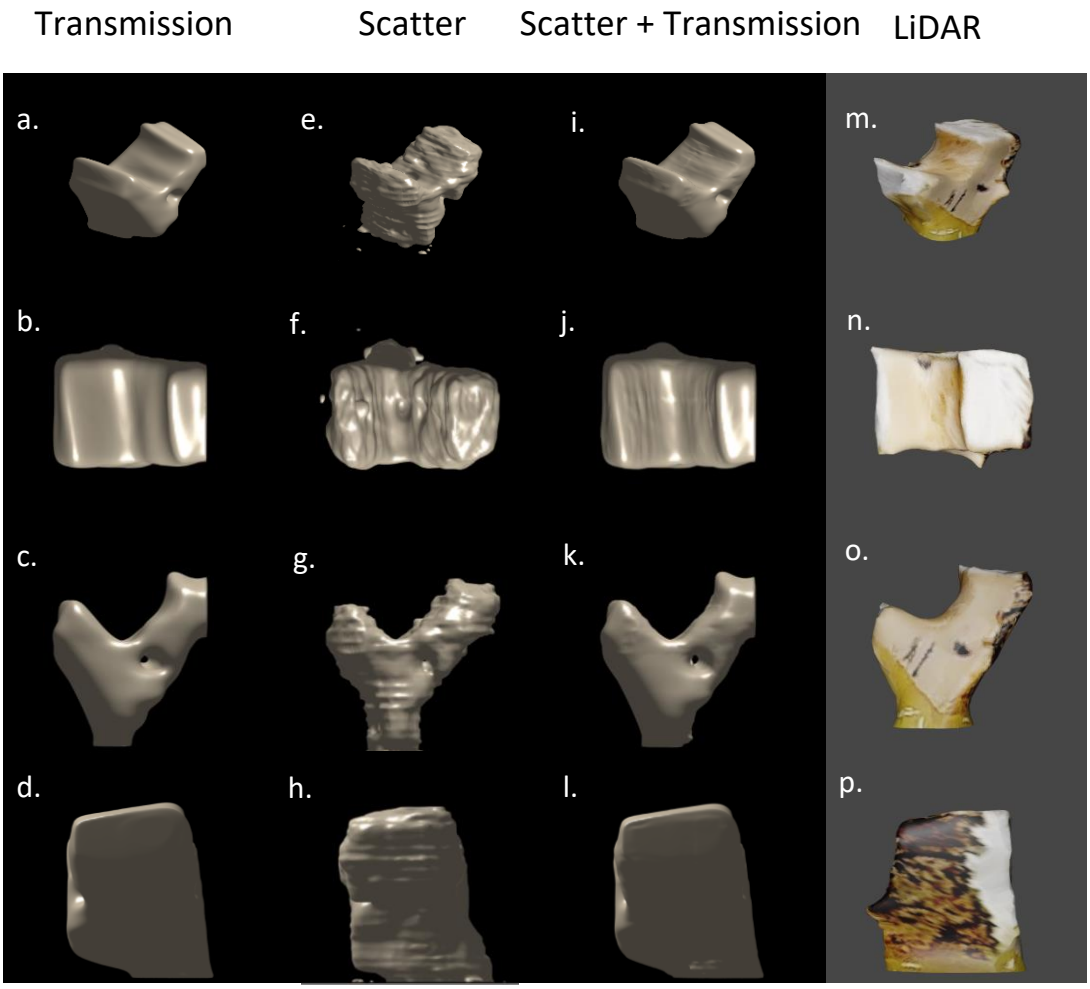

Fig. 6. Isosurface of the bone from various angles. *The isosurface was reconstructed using data obtained by different imaging modalities: (a)-(d) transmission, (e)-(h) scatter, and (i)-(l) combination of transmission and scattering. The transmission isosurface provides a general representation of the structure of the object while the scatter isosurface offers greater details thanks to its higher resolution and resilience to scattering noise. The combined isosurface shows the general structure of the object maintaining high resolution and displaying the transmission image with additional details.* As a guide I added the corresponding 3D LiDAR (laser imaging, detection, and ranging) scans captured with iPhone pro (m)-(p).

compared to the transmission reconstruction, indicating that my method has a higher resolution. The resolution of the images obtained from the transmission data is expected to be approximately 0.5 mm, which is the limit of my detector. In contrast, the resolution of my method is determined by the autocorrelation length of the mask used to generate the SI and the reconstruction algorithm as discussed in 2.2. In my case, this length is 155 μm, explaining the superior resolution observed in the scatter reconstruction.

In Fig. 6, the combined reconstruction reveals previously blurred features in the transmission reconstruction caused by scattering. This suggests a new approach to eliminate the need for collimators after the object while maintaining high-quality images despite scattering. Adopting this approach has the potential to significantly reduce radiation exposure as collimators absorb a substantial amount of radiation, which in turn requires an increase in patient dose.

5.2. Tomogram (cross-sectional) images reconstruction

Unlike previous work of 3D reconstructions with single-pixel detectors with light [51,52], which recovered only the surface gradients to derive the 3D surface of the object, I reconstructed a 3D volume that contains information about both the internal parts and the surface of the object. This enables us to present tomogram slices from top to bottom of the object as is shown in Fig. 7. In particular, I focused on a small hole in the bone, which measures approximately 2 mm on one end and 1.2 mm on the other. The images demonstrate that the edge of the hole nearly disappears in the transmission tomogram due to scattering, while the scatter tomogram remains resilient to this effect and clearly displays the hole. (Fig. 7j, Fig. 7k).

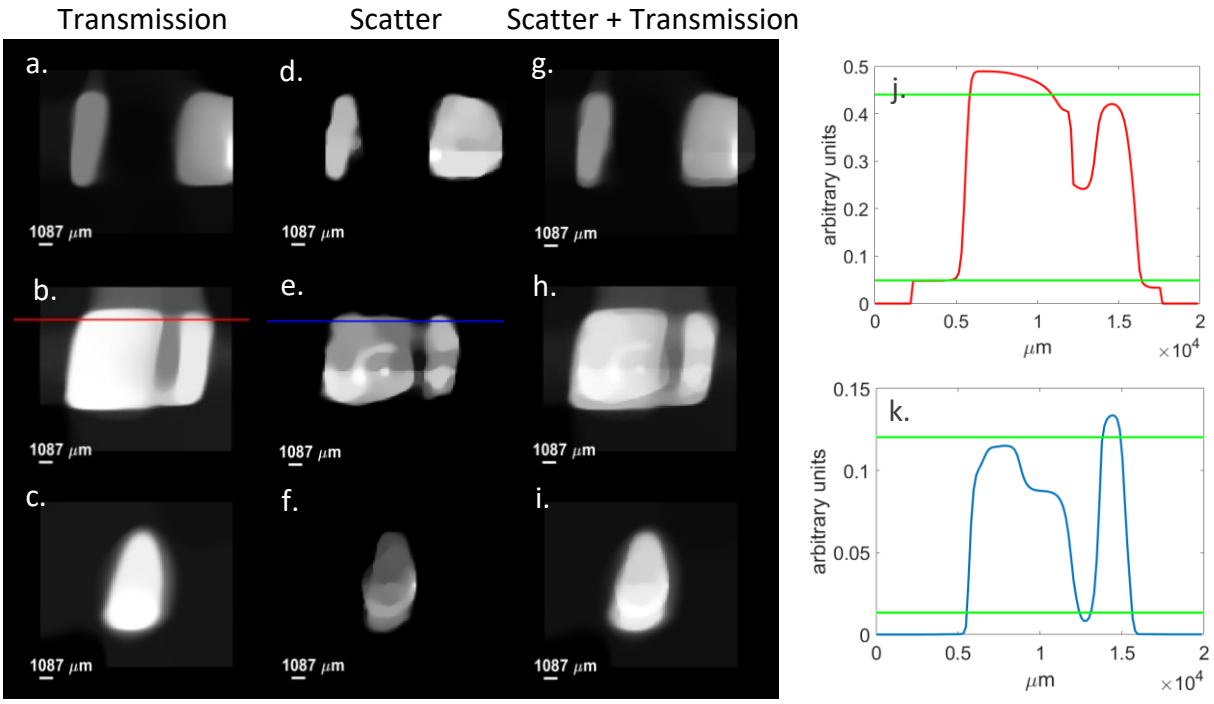

Fig. 7. Tomogram (cross-sectional) images of the bone sliced top to bottom. Tomograms from top to bottom: (a)-(c) transmission (d)-(f), scatter, and (g)-(i) a combination of both. The tomograms in each row correspond to the same slice that has been reconstructed using the respective modality. (j) and (k) presents the cross sections of (b) and (e) respectively.

6. Discussion

While in Figs 6 and 7 I have demonstrated the potential advantages of my method, it faces several challenges that need to be addressed. To illustrate some of these challenges I plot in Fig. 8 a tomogram of the bone taken from front to back and reconstructed with the three approaches. One noticeable difference is that with my method the object seems darker in the middle of the object. This is mostly due to self-absorption and self-scattering that led to a reduction of the signal measured by the detector. This challenge can be mitigated by using another detector (or detectors) at a different angle to compensate for this effect as discussed in 3.3. I also note that in the tomogram reconstructed by the combination of scattering and transmission the self-attenuation is less pronounced suggesting that the that modality can overcome the challenge with some improvement in the algorithms. A second challenge is related to the tradeoff between the measurement time and the image quality. Since my method relies on scanning, the measurement time is proportional to the number of realizations. However, to achieve high image quality, even with clever reconstruction algorithms the quality of the image is degraded when the number of realizations is much lower than the number of pixels.

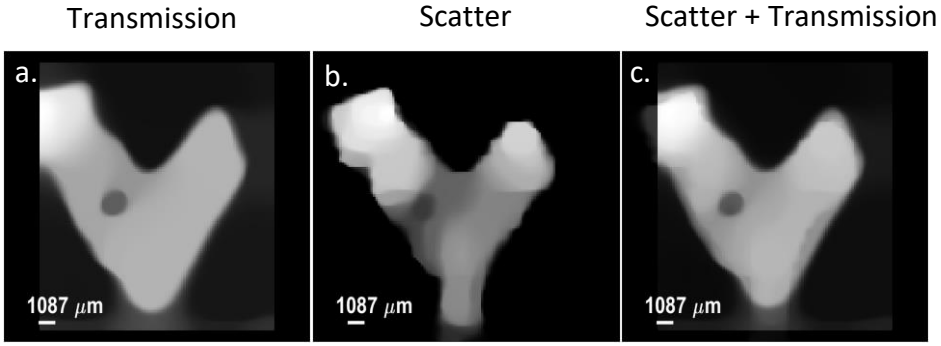

Fig. 8. Tomogram (cross-sectional) images of the bone sliced front to back. Tomograms of the front of the bone reconstructed by: (a) the transmission, (b) scatter, and (c) a combination of both.

In summary my work suggests that scatter radiation can be harnessed to create high resolution CT images, either on its or in conjunction with traditional transmission information, resulting in a significant improvement in image quality. The selection of approach depends on the specific details of the application and constraints of the measurements. For instance, using scattering-only based CT allows the detector to be mounted at any angle, which can be advantageous in situations where access to certain locations is limited. By combining scatter and transmission information, it is likely that a smaller number of scanning points will be required, making this approach more suitable when dose is a primary concern.

7. Bibliography

[1] Dinca D-C, Schubert J R and Callerame J 2008 X-ray backscatter imaging *Proc.SPIE* vol 6945 p 694516

[2] Huang S, Wang X, Chen Y, Xu J, Tang T and Mu A B 2019 Modeling and quantitative analysis of X-ray transmission and backscatter imaging aimed at security inspection *Optics Express, Vol. 27, Issue 2, pp. 337-349* **27** 337–49

[3] Chen Q, Chamoli S K, Yin P, Wang X and Xu X 2019 Active Mode Single Pixel Imaging in the Highly Turbid Water Environment Using Compressive Sensing *IEEE Access* **7** 159390–401

[4] Wu H, Zhao M, Li F, Tian Z and Zhao M 2020 Underwater polarization-based single pixel imaging *J Soc Inf Disp* **28** 157–63

[5] Li C, Yin W, Jiang H, Zhang Y, Li C, Yin W, Zhang Y and Jiang H 2013 An efficient augmented Lagrangian method with applications to total variation minimization *Comput Optim Appl* **56** 507–30

[6] Klein Y, Sefi O, Schwartz H and Shwartz S 2022 Chemical element mapping by x-ray computational ghost fluorescence *Optica* **9** 63–70

[7] Anon Industrial 3D Printing of Electronics for Manufacturing and AME

[8] Wang F, Wang C, Chen M, Gong W, Zhang Y, Han S and Situ G 2022 Far-field super-resolution ghost imaging with a deep neural network constraint *Light: Science & Applications 2022 11:1* **11** 1–11

[9] Jia X, Lou Y, Lewis J, Li R, Gu X, Men C, Song W Y and Jiang S B 2011 GPU-based fast low-dose cone beam CT reconstruction via total variation *J Xray Sci Technol* **19** 139–54

[10] Röntgen W K 1895 Über eine neue Art von Strahlen: vorläufige Mitteilung *Sitzungsber. Phys. Med. Gesell.*

[11] Barnes G T 1991 Contrast and scatter in x-ray imaging. *https://doi.org/10.1148/radiographics.11.2.2028065* **11** 307–23

[12] Wilsey R B 1922 Scattered X-rays in x-ray photography *J Franklin Inst* **194** 583–96

[13] Wilsey R B 1934 Scattered Radiation in Roentgenography of the Chest *https://doi.org/10.1148/23.2.198* **23** 198–201

[14] Luboshez B E 1927 Contrast and Fog in Radiography *British Journal of Radiology: BIR Section* **32** 1–11

[15] Lin E C 2010 Radiation Risk From Medical Imaging *Mayo Clin Proc* **85** 1142–6

[16] Ferrero A, Takahashi N, Vrtiska T J, Krambeck A E, Lieske J C and McCollough C H 2019 Understanding, justifying, and optimizing radiation exposure for CT imaging in nephrourology *Nature Reviews Urology 2019 16:4* **16** 231–44

[17] Pearce M S, Salotti J A, Little M P, McHugh K, Lee C, Kim K P, Howe N L, Ronckers C M, Rajaraman P, Craft A W, Parker L and De González A B 2012 Radiation exposure from CT scans in childhood and subsequent risk of leukaemia and brain tumours: a retrospective cohort study *The Lancet* **380** 499–505

[18] Miglioretti D L, Johnson E, Williams A, Greenlee R T, Weinmann S, Solberg L I, Feigelson H S, Roblin D, Flynn M J, Vanneman N and Smith-Bindman R 2013 The Use of Computed Tomography in Pediatrics and the Associated Radiation Exposure and Estimated Cancer Risk *JAMA Pediatr* **167** 700–7

[19] Berrington De González A, Mahesh M, Kim K P, Bhargavan M, Lewis R, Mettler F and Land C 2009 Projected Cancer Risks From Computed Tomographic Scans Performed in the United States in 2007 *Arch Intern Med* **169** 2071–7

[20] Boutis K, Cogollo W, Fischer J, Freedman S B, David G Ben and Thomas K E 2013 Parental Knowledge of Potential Cancer Risks From Exposure to Computed Tomography *Pediatrics* **132** 305–11

[21] Zhu L, Xie Y, Wang J and Xing L 2009 Scatter correction for cone-beam CT in radiation therapy *Med Phys* **36** 2258–68

[22] Zhu L, Bennett N R and Fahrig R 2006 Scatter correction method for X-ray CT using primary modulation: Theory and preliminary results *IEEE Trans Med Imaging* **25** 1573–87

[23] Ning R, Tang X and Conover D 2004 X-ray scatter correction algorithm for cone beam CT imaging *Med Phys* **31** 1195–202

[24] Rührnschopf E P and Klingenbeck K 2011 A general framework and review of scatter correction methods in x-ray cone-beam computerized tomography. Part 1: Scatter compensation approaches *Med Phys* **38** 4296–311

[25] Siewerdsen J H, Daly M J, Bakhtiar B, Moseley D J, Richard S, Keller H and Jaffray D A 2006 A simple, direct method for x-ray scatter estimation and correction in digital radiography and cone-beam CT *Med Phys* **33** 187–97

[26] Mazurov A I and Potrakhov N N 2015 Effect of Scattered X-Ray Radiation on Imaging Quality and Techniques for Its Suppression* *Biomed Eng (NY)* **48** 241–5

[27] Watson P G F, Mainegra-Hing E, Tomic N and Seuntjens J 2015 Implementation of an efficient Monte Carlo calculation for CBCT scatter correction: phantom study *J Appl Clin Med Phys* **16** 216–227–216–227

[28] Gong H, Yan H, Jia X, Li B, Wang G and Cao G 2017 X-ray scatter correction for multi-source interior computed tomography *Med Phys* **44** 71–83

[29] Mainegra-Hing E and Kawrakow I 2008 Fast Monte Carlo calculation of scatter corrections for CBCT images *J Phys Conf Ser* **102** 012017

[30] Wilkins S W, Gureyev T E, Gao D, Pogany A and Stevenson A W 1996 Phase-contrast imaging using polychromatic hard X-rays *Nature 1996 384:6607* **384** 335–8

[31] Booij R, Budde R P J, Dijkshoorn M L and van Straten M 2020 Technological developments of X-ray computed tomography over half a century: User's influence on protocol optimization *Eur J Radiol* **131** 109261

[32] Anon XCOM: Photon Cross Sections Database | NIST

[33] Rehani M M and Berry M 2000 Radiation doses in computed tomography *BMJ* **320** 593–4

[34] Brenner D J and Hall E J 2007 Computed Tomography — An Increasing Source of Radiation Exposure *New England Journal of Medicine* **357** 2277–84

[35] Klein O and Nishina Y 1928 The Scattering of Light by Free Electrons according to Dirac's New Relativistic Dynamics *Nature 1928 122:3072* **122** 398–9

[36] Lane T J, Lane T J, Ratner D and Ratner D 2020 What are the advantages of ghost imaging? Multiplexing for x-ray and electron imaging *Optics Express, Vol. 28, Issue 5, pp. 5898-5918* **28** 5898–918

[37] He Y H, Zhang A X, Li M F, Huang Y Y, Quan B G, Li D Z, Wu L A and Chen L M 2020 High-resolution sub-sampling incoherent x-ray imaging with a single-pixel detector *APL Photonics* **5**

[38] He Y H, Zhang A X, Yu W K, Chen L M and Wu L A 2020 Energy-Selective X-Ray Ghost Imaging *Chinese Physics Letters* **37** 044208

[39] Klein Y, Sawhney K, Shwartz S, Schori A and Dolbnya I P 2019 X-ray computational ghost imaging with single-pixel detector *Optics Express, Vol. 27, Issue 3, pp. 3284-3293* **27** 3284–93

[40] Klein Y, Strizhevsky E, Shwartz S, Dolbnya I P and Sefi O 2020 X-ray imaging of fast dynamics with single-pixel detector *Optics Express, Vol. 28, Issue 17, pp. 24568-24576* **28** 24568–76

[41] Schori A and Shwartz S 2017 X-ray ghost imaging with a laboratory source *Opt Express* **25** 14822

[42] Shapiro J H and Erkmen B I 2010 Ghost imaging: from quantum to classical to computational *Advances in Optics and Photonics, Vol. 2, Issue 4, pp. 405-450* **2** 405–50

[43] Chan W L, Charan K, Takhar D, Kelly K F, Baraniuk R G and Mittleman D M 2008 A single-pixel terahertz imaging system based on compressed sensing *Appl Phys Lett* **93**

[44] Pelliccia D, Rack A, Scheel M, Cantelli V and Paganin D M 2016 Experimental X-Ray Ghost Imaging *Phys Rev Lett* **117** 113902

[45] He Y-H, 何雨航, Zhang A-X, 张艾昕, Yu W-K, 俞文凯, Chen L-M, 陈黎明, Wu L-A and 吴令安 2020 Energy-Selective X-Ray Ghost Imaging * *Chinese Physics Letters* **37** 044208

[46] He Y H, Zhang A X, Li M F, Huang Y Y, Quan B G, Li D Z, Wu L A and Chen L M 2020 High-resolution sub-sampling incoherent x-ray imaging with a single-pixel detector *APL Photonics* **5** 056102

[47] Klein Y, Sawhney K, Shwartz S, Schori A and Dolbnya I P 2019 X-ray computational ghost imaging with single-pixel detector *Optics Express, Vol. 27, Issue 3, pp. 3284-3293* **27** 3284–93

[48] Zhou K C and Horstmeyer R 2020 Diffraction tomography with a deep image prior *Opt Express* **28** 12872

[49] Gatti A, Brambilla E, Bache M and Lugiato L A 2004 Ghost imaging with thermal light: comparing entanglement and classical correlation *Phys Rev Lett* **93**

[50] Biguri A, Dosanjh M, Hancock S and Soleimani M 2016 TIGRE: a MATLAB-GPU toolbox for CBCT image reconstruction *Biomed Phys Eng Express* **2** 055010

[51] Stellinga D, Phillips D B, Mekhail S P, Selyem A, Turtaev S, Čižmár T and Padgett M J 2021 Time-of-flight 3D imaging through multimode optical fibers *Science (1979)* **374** 1395–9

[52] Sun B, Edgar M P, Bowman R, Vittert L E, Welsh S, Bowman A and Padgett M J 2013 3D computational imaging with single-pixel detectors *Science (1979)* **340** 844–7

תקציר

שיטות הדמיית רנטגן מסחריות מודדות את קרני הרנטגן שעוברות בגוף, המשמשות ליצירת תמונה מפורטת של גופו או איבריו של המטופל. כאשר קרינת הרנטגן מקיימת אינטראקציה עם האטומים בגוף המטופל היא מתפזרת ופוגעת באיכות התמונה על ידי הפחתת הניגודיות והחדות שלה. מסיבה זו, קרינת רנטגן מפוזרת נחשבת בדרך כלל כמקור לרעש, ולכן סורקי רנטגן מודרניים משתדלים למזער את השפעתה על ידי הצבת רשתות וקולימטורים בין גוף המטופל למצלמה. זה מאפשר לתמונות להיות בניגודיות גבוהה יותר אך במחיר של חשיפה מוגברת עבור המטופל בגלל שחלק עיקרי מן הקרינה נחסם לפני הגעה למצלמה. ההשפעות של תופעות אלו דומיננטית אפילו יותר בסריקות טומוגרפיה ממוחשבת רפואית (CT), מכיוון שעבורן יש לצלם מספר תמונות רנטגן על מנת לשחזר תמונה תלת ממדית.

ניסיונות מרובים להשתמש בקרינה המפוזרת להדמיה פותחו בעבר אך אף אחד מהם אינו מתאים להדמיה רפואית מכיוון שהרזולוציה המושגת על ידי מכשירים אלו נמוכה מדי.

מטרתו העיקרית של המחקר שלי הייתה להראות שאפשר לנצל את הקרינה המפוזרת להדמיה ברזולוציה גבוהה במקום לחסום אותה. תכננתי להשתמש בשיטת הדמיית רפאים חישובית (CGI). שיטה זו היא שיטת הדמיה של פיקסל בודד שהוכח כי היא חסינה יותר לפיזור משיטות הדמיה סטנדרטיות. הסיבה לכך היא שב-CGI המידע המרחבי נגזר מהאינטראקציה בן הקרן המאופננת מרחבית והאובייקט, ולא מהפיקסלים של הגלאי.

בתחילת המחקר שלי, השתמשתי במקור רנטגן של 20 קילו אלקטרון וולט שלא ניתן להשתמש בו ברפואה ובביולוגיה מכיוון שבמקור שפופרת רנטגן מן הסוג הזה, רוב הקרינה נפלטת מאנודת הנחושת שלו באנרגיה של 8 קילו אלקטרון וולט, שהיא נמוכה מדי. השתמשתי במצלמת רנטגן לאנרגיות נמוכות בעלת רזולוציה של 4.5 מיקרומטר כדי לצלם תמונות של מסכה העשויה נייר זכוכית עבור הניסוי שלי. בהמשך, לאחר הרבה ניסיונות כושלים עקב פיזור ממקורות לא ידועים, הצלחתי לחסום את הקרינה המפוזרת הלא ידועה שהפריעה לי עם יריעות עופרת ולקבל מדידות טובות. לאחר מכן השתמשתי באלגוריתם TVAL3 כדי לשחזר לראשונה תמונה באיכות גבוהה, 6 מ״מ על 6 מ״מ, ברזולוציה של מתחת ל200 מיקרומטר, של אובייקט הפלסטיק שלי בצורת האות 7. בחרתי ב-TVAL3 מכיוון שהוא הוכח היטב וכבר נעשה בו שימוש בעבר כדי להפחית את זמן המדידה בניסוים נוספים שעושים שימוש ב CGI עבור שחזור תמונות ב x-ray.

למרות שהיו לי תוצאות משביעות רצון שהתקבלו לכנס CLEO 2023, מכונת ההדמיה החדשה באנרגיה גבוהה (80 קילו ולט-פיק) הגיעה למעבדה שלנו ורציתי לקחת את המחקר שלי צעד אחד קדימה על ידי שימוש בקרינה באנרגית פוטון גבוהה, שיכולה לשמש להדמיה רפואית וביולוגית. כאשר עברתי למכונה החדשה נתקלתי בקושי חדש. מצלמת הרנטגן החדשה באנרגיה גבוהה הייתה ברזולוציה נמוכה בהרבה (205 מיקרומטר) ולא יכולתי לצלם תמונות של המסכה כפי שעשיתי בניסוי האחרון. כדי להתגבר על זה, הייתי צריך להשתמש במסכה ידועה מראש במקום. השתמשתי בשירות של Nano-Dimension מכיוון שיכולתי להשתמש בטכנולוגיית מדפסת התלת מימד שלהם, המשמשת בדרך כלל להדפסת מעגלים חשמליים עם כסף, כדי לייצר מסכה מתמונה שיצרתי במחשב שלי. יצירת מסכה שניתן להשתמש בה באנרגיית פוטון גבוה היא מאתגרת מכיוון שעומק החדירה של הקרינה ארוך יותר. השתמשתי בכסף כחומר המסכה שכן הוא מסוגל לחסום כמות מספקת של קרינה. בזמן שניסיתי להשתמש במסכה גיליתי שהיא לא הומוגנית כמו העיצוב שלי בגלל שגיאות ייצור, ולא יכולתי לייצר איתה נתונים שמישים. התגברתי על זה על ידי צילום תמונות ברזולוציה נמוכה של המסכה ונרמלתי את הנתונים איתה. רק לאחר מכן יכולתי לשחזר תמונה של

עצם פרה בגודל של 20 מ״מ על 20 מ״מ, עם רזולוציה של מתחת ל200 מיקרומטר. השחזור אומנם צלח אבל לא היה מספק שכן שהאובייקט היה גדול מדי ומסובך מדי עבור רזולוציית המסכה החדשה (108 מיקרומטר). מכיוון שבתמונה היו יותר מדי פיקסלים בהשוואה למספר המדידות שהצלחתי לבצע בזמן סביר, התוצאה הסופית הייתה תמונה באיכות נמוכה ובניגודיות נמוכה. בגלל ש TVAL3 אינו מתקדם מספיק, הייתי חייב לעבור לאלגוריתם אחר. לאחר מחקר מקיף הצלחתי להתאים אלגוריתם מבוסס למידה עמוקה (GIDC) לשימושי. GIDC נועד לשמש לשיפור רזולוציה של הדמיה בשדה רחוק באור נראה, מאוד שונה מהניסוי שלי, אבל הצלחתי לנצל אותו על ידי שינוי אלמנטים בפונקציית ההפסד של הקוד. האלגוריתם החדש אפשר לי להשיג שחזור תמונה הרבה יותר טוב.

בשלב זה, שוב, בחרתי לקחת את המחקר שלי צעד נוסף קדימה ושחזרתי תמונת CT שניתן להשתמש בה לאבחון מצבים רפואיים מסובכים בחולים. לשם כך השתמשתי ב-TIGRE, ארגז כלים מבוסס מעבד גרפי עבור שחזור איטרטיבי, כדי לשחזר CT תלת ממדי. כדי ליצור את תמונת ה-CT, סובבתי את האובייקט על במה ושחזרתי 28 תמונות פיזור שונות. לאחר מכן עם TIGRE השתמשתי באלגוריתם האיטרטיבי SART-TV כדי לשחזר את תמונת ה-CT התלת-ממדית.

לסיכום, השגתי את כל מטרות המחקר שלי ויותר. שחזרתי עם קרינת רנטגן מפוזרת באנרגיה גבוהה תמונת CT תלת ממדית של עצם יונק גדול ברזולוציה של מתחת ל-200 מיקרומטר, טובה יותר מרוב שיטות ההדמיה בקרני רנטגן מפוזרות. המחקר שלי חושף טכניקה מבטיחה לשילוב נתוני קרינה מפוזרת בסריקות CT, וכתוצאה מכך שיפור ברזולוציית התמונה והפחתת מינון הקרינה למטופלים. במחקר שלי אני מוכיח שניתן להשתמש בקרינת רנטגן מפוזרת כדי לשחזר תמונות טומוגרפיה ממוחשבת ברזולוציה גבוהה עם דגימות ביולוגיות.

עבודה זו נעשתה בהדרכתו של

פרופ׳ שרון שוורץ

מהמחלקה לפיזיקה של אוניברסיטת

בר-אילן

אוניברסיטת בר-אילן

טומוגרפיה ממוחשבת ברזולוציה גבוהה של קרינת רנטגן מפוזרת עם גלאי פיקסל בודד

עדי בן יהודה

עבודה זו מוגשת כחלק מהדרישות לשם קבלת תואר מוסמך
במחלקה לפיזיקה של אוניברסיטת בר-אילן

רמת גן תשפ״ג